ISSN 1560-3547, Regular and Chaotic Dynamics, 0000, Vol. 00, No. 0, pp. 1–17. © RCD Editorial Office, 2016.

Circular vortex arrays in generalised Euler's and quasi-geostrophic dynamics

Jean N. Reinaud[1*]

[1] *University of St Andrews*
Mathematical Institute, North Haugh, St Andrews, UK

Received January 3, 2022; revised Month XX, 20XX; accepted Month XX, 20XX

Abstract—We investigate the stability of circular point vortex arrays and their evolution when their dynamics is governed by the generalised two-dimensional Euler's equations and the three-dimensional Quasi-Geostrophic equations. These sets of equations offer a family of dynamical models depending continuously on a single parameter β which sets how fast the velocity induced by a vortex falls away from it. In this paper, we show that the differences between the stability properties of the *classical* two-dimensional point vortex arrays and the *standard* quasi-geostrophic vortex arrays can be understood as a bifurcation in the family of models. For a given β, the stability depends on the number N of vortices along the circular array and on the possible addition of a vortex at the centre of the array. On a practical point of view, the most important vortex arrays are the stable ones, as they are robust and long-lived. Unstable vortex arrays can however lead to interesting and convoluted evolutions, exhibiting quasi-periodic and chaotic motion. We briefly illustrate the evolution of a small selection of representative unstable vortex arrays.

MSC2010 numbers: 76B47,76E20

DOI: 10.0000/S1560354700000012

Keywords: Point vortices dynamics, generalised Euler's equations, quasi-geostrophy

1. INTRODUCTION

Circular vortex arrays are historically one of the first configurations of point vortices ever studied in the literature. They attracted Thomson's (Lord Kelvin, [1]) attention via the analogous behaviour of floating magnets studied experimentally by Mayer [2]. The linear stability of planar two-dimensional (2D) circular vortex arrays was first analysed by Thomson [3]. Arrays of $N < 7$ vortices are linearly stable, see [3]. For $N = 7$ [4, 5] showed that the array was linearly stable (but one of the modes with a zero complex frequency). The full stability of the 7-vortex array, including nonlinear effects, was proved by [6]. The study of circular vortex arrays was also extended to geophysical flows, first in quasi-geostrophic shallow water, see [7]. In this study the authors also considered the influence of an additional vortex located at the centre of the array. Numerous additional studies have been performed on circular vortex arrays, sometimes also referred to as vortex N-gons, see the literature reviews proposed in [8] and [9]. Other studies include (i) variations on problem geometry such as the studies of vortex array inside and outside a circle, see [10, 11], and on the surface of a sphere [12, 13], and (ii) variations on the physical model, such as vortices in a Bose–Einstein condensate [14].

More recently, Reinaud [15] considered circular vortex arrays in the three-dimensional quasi-geostrophic (3DQG) regime. Both point vortex arrays and finite-volume vortex arrays were considered in that study. The study was recently further extended to include the influence of the vortex height-to-width vortex ratio on the stability of finite-volume vortex arrays, see [16]. In [15] it is showed that circular arrays of only $N \leq 5$ point vortices are linearly stable in the 3DQG regime. It should be noted that an analogous problem of arrays of negative electric charges placed

*E-mail: jean.reinaud@st-andrews.ac.uk

in a uniformly electrified sphere was addressed in [17]. Additionally the problem of staggered vortex arrays is addressed in [8] while [18] addresses the effects of an exponential density stratification.

The main difference between the dynamics of the standard 2D and 3DQG regimes is how fast the velocity induced by a point vortex falls away from it. It falls as r^{-1} in 2D while it falls as r^{-2} in 3DQG. Here r is the distance between the point vortex and the point where the velocity is evaluated. The main motivation of the study is to have a deeper understanding of the similarities and the differences between the 2D and 3DQG regimes by introducing a family of models where the velocity induced by a vortex falls as $r^{-(\beta+1)}$, $0 \leq \beta \leq 3$. For example, we show in this study that circular arrays of $N = 5$ point vortices are stable for all β, while arrays of $N = 6$ are stable for $\beta < 0.9673$ and unstable otherwise. For $N = 7$ only the standard 2D Euler circular vortex arrays, corresponding to $\beta = 0$, are stable. We also investigate the influence of an additional central vortex on the stability of the arrays. We show for example that for $N > 5$, the addition of a moderate-strength like-signed vortex array may stabilise the array. Overall, increasing β tends to make the arrays more unstable in most situations. Increasing β can however stabilise vortex arrays with an intense like-signed central vortex if $N \geq 5$. The evolution of unstable arrays may exhibit quasi-periodic motion and more often chaotic motion.

The paper is organised as follows. Section 2 describes the mathematical set-up, while the more technical details are given in an appendix. The linear stability and the evolution of circular arrays of N vortices, $2 \leq N \leq 10$, are presented in section 3. A similar analysis when an extra vortex is added at the centre of the array is presented in section 4. Conclusions are presented in section 5.

2. Mathematical setup

We consider a fluid flow whose evolution is controlled by a materially-conserved scalar field q. The scalar field q relates to a scalar streamfunction φ via a modified Poisson's equation

$$q = -(-\Delta)^{\alpha}\,\varphi. \tag{2.1}$$

In both the 2D and 3D situations, the scalar q is materially conserved through the advection by a two-dimensional (or layerwise two-dimensional) velocity field (u, v)

$$\frac{\partial q}{\partial t} + u\frac{\partial q}{\partial x} + v\frac{\partial q}{\partial y} = 0. \tag{2.2}$$

In 2D, the horizontal velocity field is the full velocity field and in 3DQG, the vertical velocity is too small to contribute to the advection of q, see [19]. In equation (2.2), the horizontal advecting velocity field (u, v) derives from the streamfunction φ,

$$u = -\frac{\partial \varphi}{\partial y}, \qquad v = \frac{\partial \varphi}{\partial x}. \tag{2.3}$$

In the standard two-dimensional Euler's equations, q is simply the vorticity, Δ stands for the two-dimensional Laplace's operator and $\alpha = 1$. In the standard 3DQG equations, q is the quasi-geostrophic potential vorticity anomaly, Δ stands for the three-dimensional Laplace's operator and $\alpha = 1$. Another classical model covered by our family of generalised models is the Surface Quasi-Geostrophic (SQG) model, see [20]. In this model, q is the potential temperature, Δ stands for the two-dimensional Laplace's operator and $\alpha = 1/2$.

Defining the positive parameter β as

$$\beta = n - 2\alpha, \;\; \text{for } \; 0 < \alpha < n/2, \tag{2.4}$$

where n is the space dimension (in practice $n = 2, 3$ for our study), equation (2.1) can be formally inverted in an infinite domain using the Green's function, given in [21],

$$G(\boldsymbol{x}; \boldsymbol{x'}) = -\frac{C_{n,-\alpha}}{|\boldsymbol{x} - \boldsymbol{x'}|^{\beta}} \tag{2.5}$$

with

$$C_{n,-\alpha} = \frac{\Gamma(n/2 - \alpha)}{4^{\alpha}\Gamma(\alpha)\pi^{n/2}}, \tag{2.6}$$

Model	n	α	β	$G(\boldsymbol{x};\boldsymbol{x}')$
2D Euler	2	1	0	$(2\pi)^{-1}\ln\lvert\boldsymbol{x}-\boldsymbol{x}'\rvert$
3D QG	3	1	1	$(4\pi\lvert\boldsymbol{x}-\boldsymbol{x}'\rvert)^{-1}$
SQG	2	1/2	1	$(2\pi\lvert\boldsymbol{x}-\boldsymbol{x}'\rvert)^{-1}$

Table 1. Parameters of the classical models in the generalised Euler's and quasi-geostrophic models.

where Γ is the standard Gamma function.

If $\alpha = n/2$,

$$G(\boldsymbol{x};\boldsymbol{x}') = C' \log|\boldsymbol{x}-\boldsymbol{x}'|, \tag{2.7}$$

where $C' = (2\pi)^{-1}$ for $n = 2$ and $(2\pi^2)^{-1}$ for $n = 3$, see [21]. In the text, we will refer to these cases as $\beta = 0$ by extension, even if, in contrast with equation (2.5), β no longer plays there the role of a power in the Green's function for the streamfunction. Yet, in the discussion that follows, this allows to identify all models from the value of β alone.

The kernel that gives the velocity field is

$$\boldsymbol{K}(\boldsymbol{x};\boldsymbol{x}') = \left(-\frac{\partial G}{\partial y}, \frac{\partial G}{\partial x}\right) = \frac{C}{|\boldsymbol{x}-\boldsymbol{x}'|^{\beta+2}} \begin{pmatrix} -(y-y') \\ x-x' \end{pmatrix} \tag{2.8}$$

where C is the constant $\beta C_{n,-\alpha}$ for $0 < \beta < n/2$ or the constant C' for $\beta = 0$. It should indeed be noted that the formula for $\boldsymbol{K}$ remains formally valid for $\beta = 0$. Overall we see that the velocity induced by a point vortex falls as $r^{-(\beta+1)}$ away from the vortex. Here, r denotes the distance. The classical 2D Euler, 3DQG and SQG models are summarised in Table 1.

In this study the scalar field q consists of an array of point vortices, i.e. singularities or Dirac distributions. We define the strength κ_i' of point vortex i the space-integrated scalar field over vortex i scaled by $C_{n,-\alpha}$ (or by C' for $\beta = 0$). Hence, for an array of N point vortices located at $\boldsymbol{x}_i$ and of strength κ_i', $1 \le i \le N$, the scalar field is

$$q(\boldsymbol{x}) = \frac{1}{C_{n,-\alpha}} \sum_{i=1}^{N} \kappa_i' \, \delta(\boldsymbol{x}-\boldsymbol{x}_i), \tag{2.9}$$

where $\delta()$ is the Dirac distribution in $\mathbb{R}^n$ and $\alpha \neq n/2$. When $\alpha = n/2$ we just replace the scaling factor $1/C_{n,-\alpha}$ by $1/C'$ in equation (2.9). The streamfunction induced by the N vortices then follows from the Green's function:

$$\varphi(\boldsymbol{x}) = -\sum_{i=1}^{N} \frac{\kappa_i'}{|\boldsymbol{x}-\boldsymbol{x}_i|^{\beta}}, \quad \forall \boldsymbol{x} \neq \boldsymbol{x}_i. \tag{2.10}$$

The flow evolution is obtained by following the vortices as they are advected by the velocity they induce on each other. Their trajectories is thus determined by integrating in time

$$\left(\frac{\mathrm{d}x_i}{\mathrm{d}t}, \frac{\mathrm{d}y_i}{\mathrm{d}t}\right) = (u_i, v_i) = \sum_{j=1, j\neq i}^{N} \frac{\kappa_j}{|\boldsymbol{x}_i-\boldsymbol{x}_j|^{\beta+2}}(-y_i+y_j, x_i-x_j), \tag{2.11}$$

where $\kappa_i = \beta\kappa_i'$ for $\beta \neq 0$ or $\kappa_i = \kappa_i'$ for $\beta = 0$ is vortex i's rescaled strength. In this study we only consider generalised 2D Euler vortex arrays or generalised 3DQG vortex arrays where all vortices lie on the same horizontal plane. This means that the distances $|\boldsymbol{x}_i - \boldsymbol{x}_j|$ in equation (2.11) are always horizontal distances, and there is no formal difference between the 2D and 3D dynamical models, for the same value of the parameter β. It should be however kept in mind that the value of the parameter β for a given value of α in equation (2.1) depends on the dimension of space n. We

consider $n = 2$ or 3 in this study, and $0 < \alpha \leq n/2 \leq 1.5$. Therefore, the full range of the parameter β is $[0, 3)$. Only the range $[0, 2)$ is applicable to the generalised 2D Euler models while the range $[2, 3)$ is only relevant to the generalised 3DQG models.

The equations for the linear stability analysis are obtained by explicitly linearising equation (2.11) with respect to perturbations to the vortex locations, about their location at equilibrium, written in the frame uniformly moving (rotating) with the equilibrium. The equations are detailed in the appendix. They result in an eigenvalue problem, where the real part σ_r of the complex eigenvalues $\sigma = \sigma_r + \mathrm{i}\sigma_i$ gives the mode's growth rate, while σ_i is the mode's frequency.

It should be noted that, for completeness, the stability analysis of a configuration under a Hamiltonian dynamics could be complemented by an analysis of the nonlinear stability, [22–24] as, for example, done in [6, 10, 11, 25] where it is shown that some linearly stable arrays may be sensitive to nonlinear instabilities.

3. N-VORTEX ARRAYS

We first consider circular vortex arrays of N identical point vortices lying equally-spaced along a circle of radius R. Without loss of generality we set $R = 1$. All vortices have a rescaled strength $\kappa_i = \kappa_p$, $1 \leq i \leq N$ and we set $\kappa_p = 1$ without loss of generality. The vortices are initially located at an azimuthal angle $\theta_i = 2\pi(i-1)/N$, hence vortex 1 lies on the semi-axis $x > 0$ at $t = 0$. By symmetry, such a circular N-vortex array is a relative equilibrium, steadily rotating at an angular velocity Ω.

We first analyse the linear stability of the circular vortex arrays by solving the eigenvalue problem described in the appendix. The analysis first shows that all circular vortex arrays with $2 \leq N \leq 5$ are linearly stable for all $\beta \in [0, 3)$. The first instability occurs for $N = 6$. The 6-vortex arrays are stable if β less than a threshold β_c and unstable for $\beta > \beta_c$, with $\beta_c \simeq 0.9673$. The maximum growth rates σ_r^m for $N = 6$ is shown vs β in figure 1. It should be noted that $\sigma = -\sigma_r^m$ is also an eigenvalue, hence there is a stable mode ($\sigma_r < 0$ not shown) associated with the unstable mode. The curve $\sigma_r^m(\beta)$ shows a bifurcation at $\beta = \beta_c$, with $0 < \beta_c < 1$. Hence, the bifurcation occurs at a value of β between the value corresponding to the 2D Euler's dynamics and the one corresponding to the 3DQG dynamics. Hence the difference between the stability of the classical 2D Euler vortex arrays ($\beta = 0$) and the standard 3DQG ($\beta = 1$) can be understood from a bifurcation in the continuous family of generalised dynamical models parametrised by β.

For $N = 7$, we recover that the array is linearly stable for $\beta = 0$, corresponding to the classical planar 2D vortex array. However, all 7-vortex arrays are unstable for $\beta > 0$, with σ_r^m/κ_p increasing with β as shown in panel (a) of figure 1. For $N > 7$, the circular vortex arrays are linearly unstable as shown in panel (b) of figure 1 for $N = 8, 9, 10$. Again, σ_r^m/κ_p increases with β in these cases.

We next illustrate the evolution of unstable circular N-vortex arrays. We start with four cases of unstable 6-vortex arrays and $\beta = 1.2$, 1.5, 2 and 2.5. Recall that the latter two cases with $\beta \geq 2$ assume that the fluid domain is three-dimensional, $n = 3$. In all cases the array is perturbed at $t = 0$ by moving vortex 1 from its equilibrium location $(x_1, y_1, z_1) = (1, 0, 0)$ to $(1 + \epsilon, 0, 0)$, with $\epsilon = 10^{-3}$. Equation (2.11) is integrated in time using a fourth-order Runge-Kutta scheme with an adaptive time-step set to $dt = 0.01/u_{max}$, where u_{max} is maximum vortex displacement velocity at time t. This choice simply controls the maximum distance travelled by a vortex within one time step to 1% of the array's radius $R = 1$.

The early trajectories of the vortices are shown in figure 2 for $0 < t < 1000$. They are plotted in the reference frame steadily rotating at the equilibrium angular velocity Ω. If the array was stable, the vortices would appear still in this reference frame. The trajectories show that the vortices oscillate radially from their equilibrium location. The oscillations modify the rotation of the array, hence we see the vortices moving in the azimuthal direction. The radial oscillations appear less regular as β increases. To further examine these oscillations we plot the evolution of the radial position $r_1 = |\boldsymbol{x}_1|$ of vortex 1 in figure 3. We observe near regular oscillations of the radial location r_1 indicating that the early evolution of the unstable 6-vortex arrays is quasi-periodic. This is not unlike the motion of the 6-vortex array for $\beta = 1$ shown in [15]. The oscillations are however less regular as β increases, including hints of doubling of the oscillations frequencies (see in particular panel (b) of figure 3 for $\beta = 1.5$). To further illustrate the long term evolution of the vortices, we

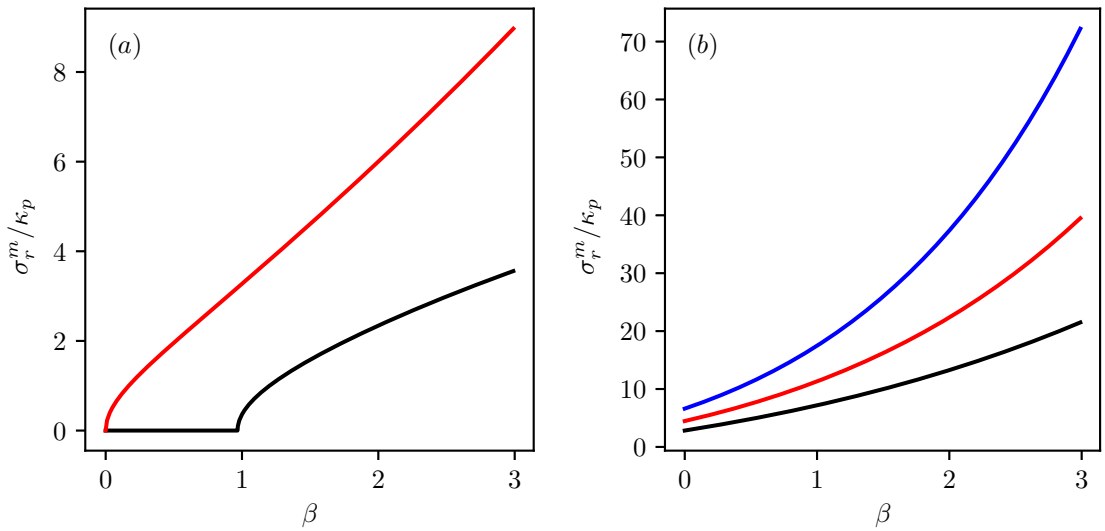

Fig. 1. Largest growth rate σ_r vs β for circular N-vortex arrays with (a) $N = 6$ (black), 7 (red), and (b) $N = 8$ (black), 9 (red) and 10 (blue).

perform a second numerical simulation using a fixed time step for simplicity, $dt = 2 \times 10^{-3}$. The value of dt is set to be less than the minimum time step used in the previous simulation with an adaptive time step. We run the simulation up to $t = 100000$, saving the location of vortex 1 in the reference frame steadily rotating at the angular velocity Ω, every time interval $\Delta t = 1$. This allows to produce a stroboscopic view on the location of vortex 1 shown in figure 4. It should be noted that the system is sensitive to the change in time step, due to the high sensitivity of the dynamical systems to perturbations, hence to numerical noise. Nonetheless the qualitative behaviour of the vortex array remains the same. Panel (a) of figure 4 shows that for $\beta = 1.5$ vortex 1 mostly oscillates within an annulus about the equilibrium radius $R = 1$. To better understand the distribution of the location of vortex 1, we measure of probably density function (pdf) of both the radial and azimuthal location of vortex 1 measured every $\Delta t = 1$. We analyse the position until $t_{max} = 100000$, hence the vortex 1 locations sample has a size $n_s = 100000$. We discretise the range of radial locations $[0, 2.025)$ into $n_b = 41$ bins of width $\delta r = 0.05$ and we count the number n_i^r of times vortex 1 had a radial location $r_1 \in [(i-1)\delta r/2, i\delta r/2)$, $1 \le i \le n_b$. Similarly we count the number n_i^θ of times vortex 1 has an azimuthal angle $\theta \in [(i-1)\delta\theta/2, i\delta\theta/2)$, where $\delta\theta = 2\pi/nb$. We define the pdf for the radius r and azimuth θ as

$$pdf(r)\,\delta r = n_i^r/n_s, \quad pdf(\theta)\,\delta\theta = n_i^\theta/n_s \tag{3.1}$$

Results are shown in panel (a) of figure 5 for $\beta = 1.5$. The pdf of r_1 is strongly peaked at $r = R = 1$, and is non-zero only in a narrow region around $R = 1$, confirming that vortex 1 mostly oscillates within a narrow annulus. The pdf of θ exhibits a couple of peaks for small θ, which is a trace of the early evolution where vortex 1 remains close to its initial equilibrium location.

For $\beta = 2.5$ the long-term evolution of vortex 1 is more complex. Not only the width of the annulus about $r = R = 1$ expands, but vortex 1 can also be found in the central region of the array, as seen from panel (b) of figure 4. The long-term evolution is chaotic in this case. We also notice that the distribution of locations appears (on average) uniform in the azimuthal direction. To understand why the vortex 1 is predominantly found in an annulus about $R = 1$ or in the central region, we may first notice that the centre of the array is a region of low velocity. Hence in the chaotic dynamics, if a vortex moves towards the centre, it is likely to slow down and remains in the central region for some time. Since the angular impulse

$$J = \frac{1}{2}\sum_{i=1}^{N}(x_i^2 + y_i^2)\,\kappa_i \tag{3.2}$$

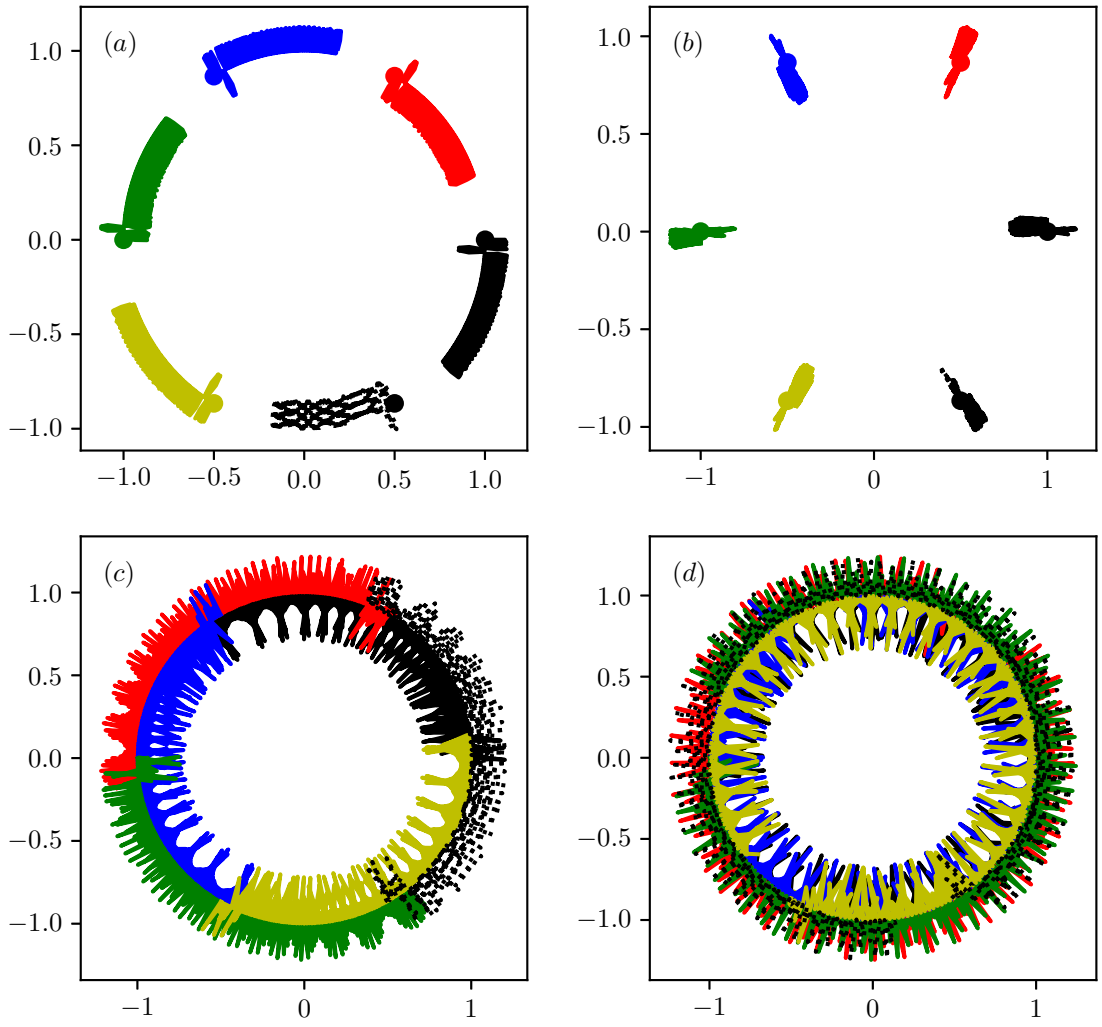

Fig. 2. Trajectories of the 6 vortices of unstable circular 6-vortex arrays in the reference frame steadily rotating at the equilibrium angular velocity Ω for (*a*): $\beta = 1.2$ and $0 \leq t \leq 996$, (*b*): $\beta = 1.5$ and $0 \leq t \leq 959$, (*c*): $\beta = 2$, $0 \leq t \leq 955$ and (*d*): $\beta = 2.5$, $0 \leq t \leq 973$.

is conserved, the migration of any vortex near the centre must be compensated by an increase of the average radial distance between the other vortices and the centre. It is therefore unlikely though not impossible, that more than one vortex at any given time would migrate towards the centre. Since there is no reason why any given vortex should remain in the central region for longer period of times than any other, each of the N vortices is likely to spend a small amount of time near the centre. This explains why the probably density function of the radius r of vortex 1 exhibit a strong peak about the initial radius $r = 1$, and a much smaller secondary peak at small r, indicating the transient times the vortex spends in the central region as confirmed in figure 5. On the other hand the *pdf* of θ is nearly flat and equal to a uniform azimuthal distribution $(2\pi)^{-1}$.

We next consider unstable circular 7-vortex arrays. Figure 6 shows the evolution of unstable 7-vortex arrays for $\beta = 0.5$, 1, 2 and 2.5. In all cases the early vortex trajectories appear chaotic. As for $N = 6$, we consider the long-term chaotic evolution of the arrays. Figure 7 shows the stroboscopic view of the location of vortex 1 for $\beta = 2.5$ with a sampling time period $\Delta t = 1$ for $0 \leq t \leq 100000$. Compared to the cases with $N = 6$ the location distribution appears more diffuse, while still exhibiting a higher location density in an annular region around $r = R = 1$ and in the central region. This is confirmed by the *pdf* of r shown in figure 8 where we recover the two peaks, one near $r = R = 1$ and the other one for small r. The distribution is indeed more diffuse and the

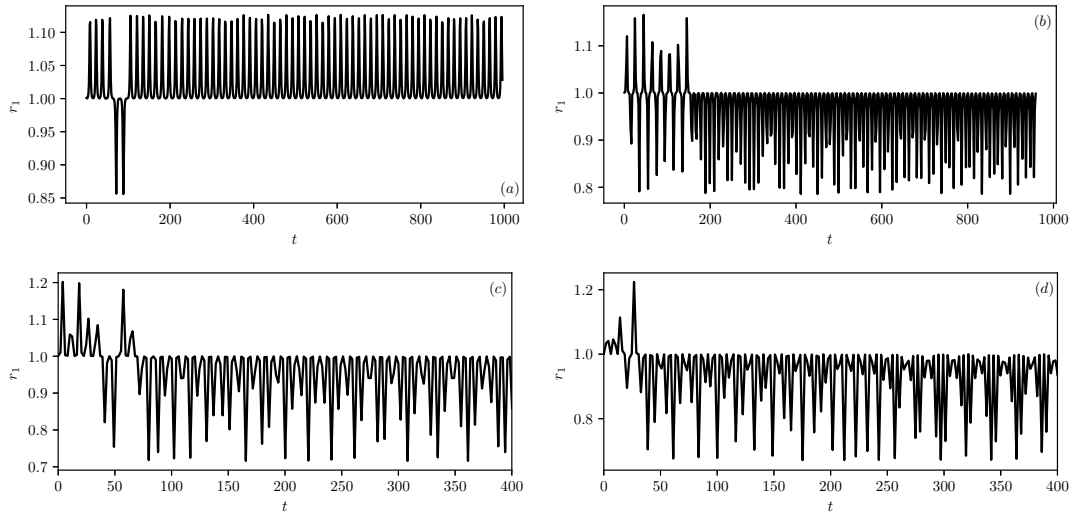

Fig. 3. Evolution of the radial position r_1 of vortex 1 for the unstable circular 6-vortex array with (a): $\beta = 1.2$ and $0 \leq t \leq 996$, (b): $\beta = 1.5$ for $0 < t < 959$, (c): $\beta = 2$ and $0 \leq t \leq 400$ and (d): $\beta = 2.5$ and $0 \leq t \leq 400$.

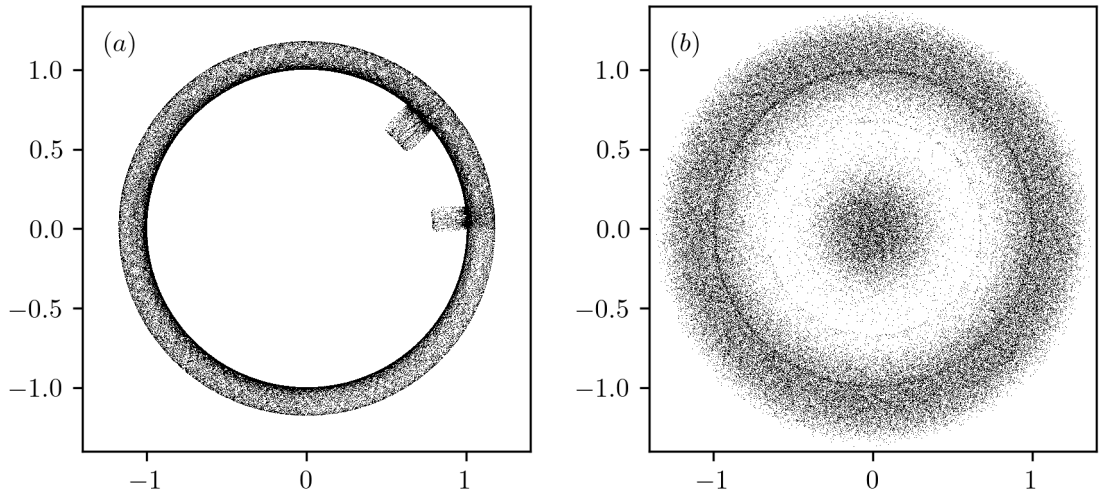

Fig. 4. Stroboscopic view of the location of vortex 1 in an unstable circular 6-vortex array in the reference frame steadily rotating at the equilibrium angular velocity Ω. A point is shown every $\Delta t = 1$ for $0 \leq t \leq 100000$ and for $\beta = 1.5$ (a) and 2.5 (b).

main peak near $r = R = 1$ less pronounced than for $N = 6$ and the same value of $\beta = 2.5$. Again, the *pdf* of azimuthal location of vortex 1 is nearly uniform and close to $(2\pi)^{-1}$.

4. $N + 1$-VORTEX ARRAYS

We next consider the influence of an additional vortex lying on the same horizontal plane as the circular N-vortex array and located at the centre of the array. Such arrays are known in the literature as $N + 1$-vortex arrays. We call the N vortices lying on the circle of radius $R = 1$ the peripheral vortices and we label them by their index $i = 1, .., N$ as in the previous section. The additional vortex is simply called the central vortex and is labelled as vortex 0. All peripheral vortices have the same rescaled strength $\kappa_i = \kappa_p = 1$, $1 \leq i \leq N$. The central vortex has a strength $\kappa_0 = \kappa_c$ which can have the same sign as or the opposite sign to κ_p.

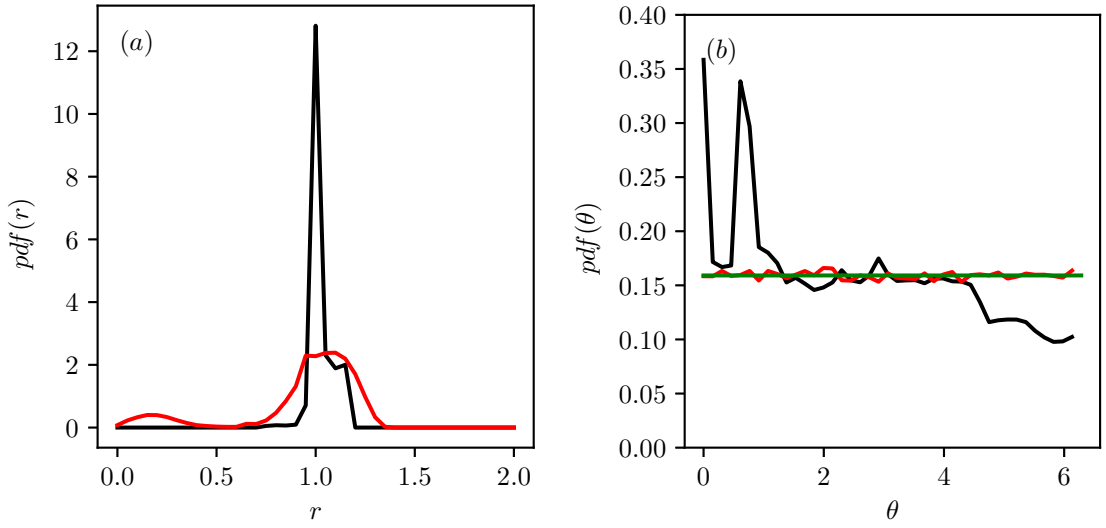

Fig. 5. Probability density function ($p.d.f$) vs r of (a) the radial location and (b) the azimuthal location of vortex 1 in a circular 6-vortex array. The location is sampled every $\Delta t = 1$ for $0 \leq t \leq 100000$ and for $\beta = 1.5$ (black) and $\beta = 2.5$ (red). The solid green line in (b) correspond to $(2\pi)^{-1}$ corresponding to an uniform azimuthal distribution.

We plot the largest growth rate σ_r^m in the plane (κ_c, β) for the $N+1$-vortex arrays for $\beta \in [0, 3)$, and $-4 \leq \kappa_c \leq 4$, and for $N = 2$, 3, 4 and 5 in figure 9, and $N = 5$, 7, 8 and 9 in figure 10 and finally $N = 10$ in figure 11. For $N = 2$, the vortex arrays are stable provided κ_c is less than a threshold typically less than $-\kappa_p$ and which depends on β. The $2+1$-vortex arrays are unstable otherwise. We notice that the $2+1$-vortex arrays are more unstable as β increases: the largest growth rate σ_r^m is larger and the region of the parameter space where the equilibria are unstable is larger. We should also note that the $2+1$-vortex array with $\kappa_c = 0$ are unstable. It may seem to contradict the results obtained for the 2-vortex arrays. These were found to be linearly stable. There is in fact no contradiction. The mode of instability captured by the linear stability analysis for $\kappa_c = 0$ only affects the (passive) central vortex which is located at a hyperbolic critical point of the flow field generated at the two (active) peripheral vortices, as already discussed in [15]. During the evolution of the unstable $2+1$-vortex array, the passive central vortex moves away from its initial, equilibrium location without affecting the peripheral vortices. For unstable $2+1$-vortex arrays with $\kappa_c \neq 0$ any motion of the central vortex however breaks the problem's symmetry and affects the peripheral vortices.

The situation is similar for $N = 3$ where the $3+1$-vortex arrays are also unstable for large κ_c. The main difference with $N = 2$ is that the threshold separating the regions of stability and instability is positive and marginally larger than κ_p. The situation changes for $N = 4$. In this case, the presence of a negative central vortex tends to destabilise the array. Again the largest growth rate σ_m^r increases with β. The $4+1$-vortex arrays are stable for low negative strength and moderate positive strength central vortices. We shall comment further on the effect of a central vortex with a large positive strength in the next paragraph. As we further increase N from $N = 5$ the vortex arrays become increasingly unstable: the typical value of the largest growth rate σ_r^m increases and the region of the parameter space where the vortex arrays are unstable increases in size in the interval $\kappa_c \in [-4, 4]$ as β increases. Moreover, the threshold in κ_c separating the region of stable and unstable vortex arrays moves towards larger values as N increases.

As seen in figure 10 for $N = 4$, the $4-$vortex arrays are unstable for large positive κ_c. We therefore extend the previous linear stability analysis to $\kappa_c > 4$ for $N \geq 4$. Results are presented in figure 12. For $N = 4$, the largest growth rate σ_r^m increases with both κ_c and β. The situation changes drastically for $N > 4$. Although there is also a second region of instability for large positive κ_c, it appears first for small β as κ_c increases, see results in figure 12 for $5 \leq N \leq 9$. The threshold in κ_c which delimits the second region of instability corresponds to increasing values of κ_c as N

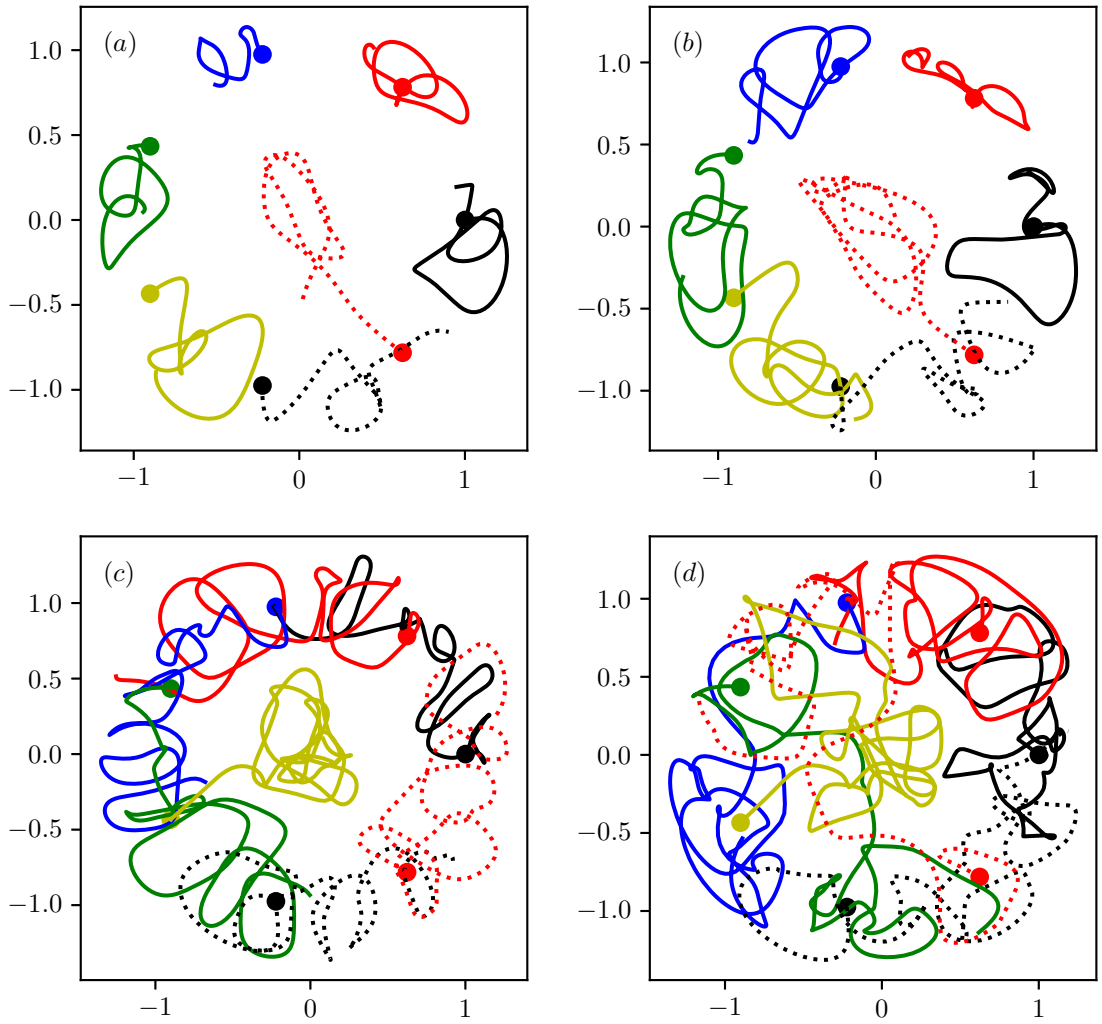

Fig. 6. Trajectories of the 7 vortices of unstable circular 7-vortex arrays in the reference frame steadily rotating at the equilibrium angular velocity Ω for (a): $\beta = 0.5$ and $0 \le t \le 9.77$, (b): $\beta = 1.0$ and $0 \le t \le 9.85$, (c): $\beta = 2$, $0 \le t \le 9.72$ and (d): $\beta = 2.5$, $0 \le t \le 9.75$.

increases. On the other hand increasing β stabilises the array more efficiently as N increases: the region of instability occupies as increasingly narrow region near $\beta = 0$ as N increases. It should also be noted that for large N, the secondary region of instability corresponds to arrays with a central vortex much more intense than the individual peripheral vortices. Hence, overall, we conclude that for $N \ge 4$, a moderate like-signed vortex stabilises the vortex array, as observed for $\beta = 1$ in [15].

We next examine the nonlinear evolution of a selection of three unstable $10 + 1$-vortex arrays with $\kappa_c = \kappa_p$. We consider $\beta = 0.5$, $\beta = 1.5$ and $\beta = 2.5$. The early vortex trajectories are shown in figure 13. The vortex trajectories show a chaotic vortex motion in all three cases. This is generic of unstable vortex arrays with a large number of like-signed vortices. The central vortex is seen to be able to move away from the centre towards the peripheral region $r \simeq R = 1$. At later times, a peripheral vortex may move temporarily towards the central region, as it was already the case for the N-vortex arrays.

Figure 14 shows a stroboscopic view of the location of vortex 1 with a sampling period of $\Delta t = 1$ and for $0 \le t \le 100000$ for the three cases. The distribution of location is qualitatively similar for the all three values of β, and also qualitatively similar to one obtained for the circular 7-vortex array with $\beta = 2.5$ described in section 3. The distribution of location appears on average uniform in the azimuthal direction. In the radial direction, there is a higher density of points in an annular

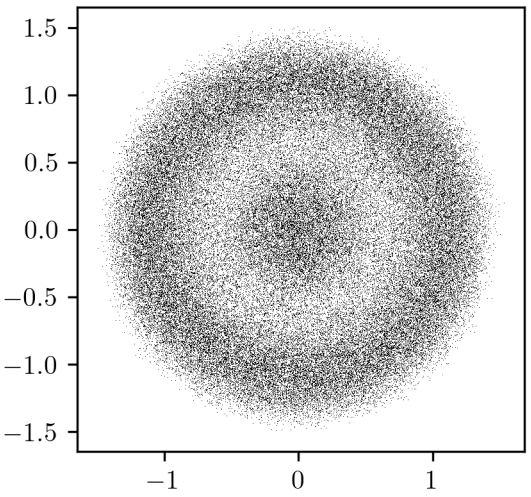

Fig. 7. Stroboscopic view of the location of vortex 1 in an unstable circular 7-vortex array in the reference frame steadily rotating at the equilibrium angular velocity Ω. A point is shown every $\Delta t = 1$ for $0 \leq t \leq 100000$ and for $\beta = 2.5$.

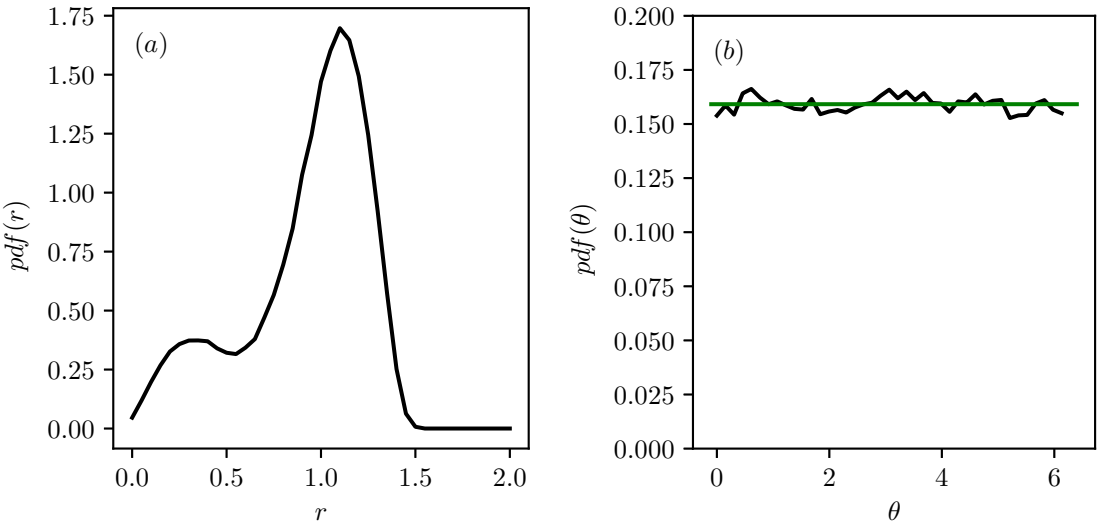

Fig. 8. *p.d.f* of radial and azimuthal location of vortex 1 in a circular 7-vortex array. The location is sampled every $\Delta t = 1$ for $0 \leq t \leq 100000$ and for $\beta = 2.5$. The solid green line in (b) correspond to $(2\pi)^{-1}$ corresponding to an uniform azimuthal distribution.

region around the initial radius $r = R = 1$ and in the central region. As β increases, the distribution appears more diffuse. This is confirmed by the *pdf* of r presented in figure 15. The main peak of the *pdf* of r, which remains about $r = R = 1$ for all three cases, decreases as β increases. Its base also broadens. Moreover the *pdf* of r in the intermediate region between the central region and the main peak increases as β increases. This is an indication that the motion becomes more chaotic. Similarly to the other cases, the azimuthal distribution is nearly uniform with $pdf(\theta) \simeq (2\pi)^{-1}$.

In the previous examples, the vortices remain confined within a disk centred at the origin. This is a consequence of the invariance of the angular impulse J for the like-signed vortices. In the case of a negative central vortex, the constraint on J can be less restrictive. An example of evolution of an unstable $10 + 1$-vortex array with $\kappa_c = -\kappa_p$ and $\beta = 2$ is shown in figure 16. As in the previous

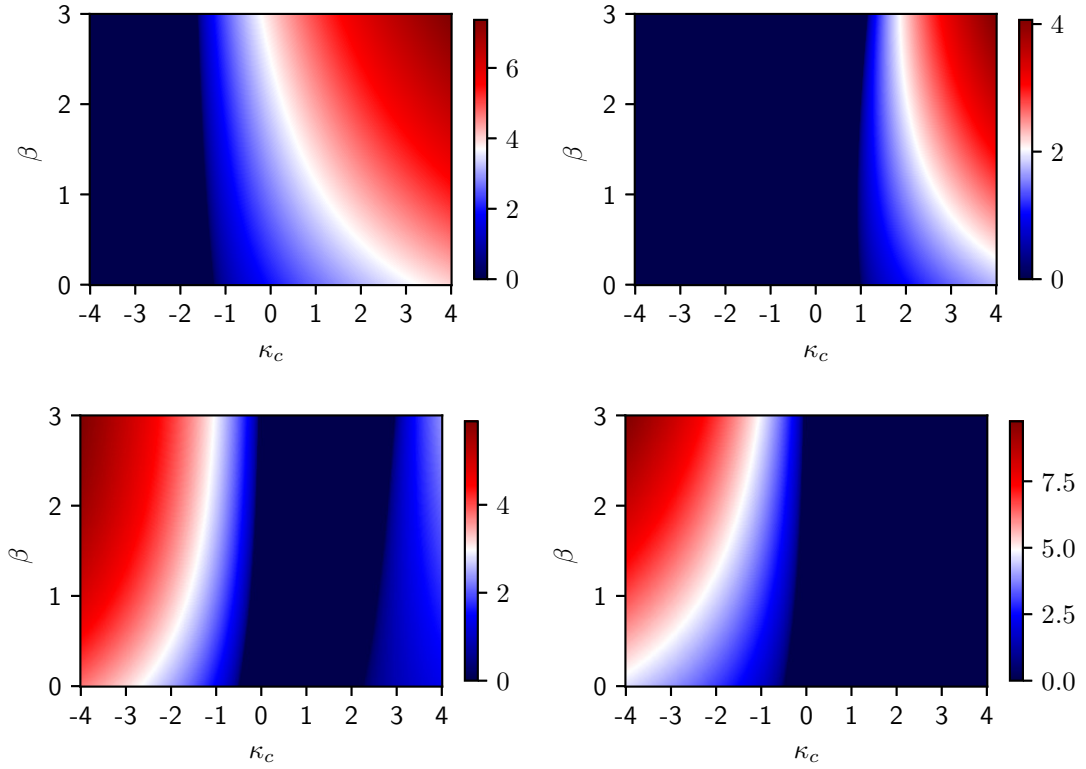

Fig. 9. Largest growth rate σ_r^m/κ_p in the (κ_c, β)-plane for a circular $N+1$-vortex array with $N=2$ (top left), 3 (top right), 4 (bottom left) and 5 (bottom right).

case, the vortices first exhibit a chaotic motion. Eventually the central vortex pairs with one of the peripheral vortex to create a vortex dipole of zero net strength. The pairing is due to the two vortices getting first close together and induce onto each other a large velocity which makes the pair move away rapidly from the other vortices. The influence of the other vortices on the dipolar pair therefore weakens and the dipolar pair continues to self-propagate. Since the dipolar pair has zero net strength, it contributes very little to the net angular impulse of the flow. The dipolar pair can therefore move very far away from the centre of the domain while the angular impulse remains conserved. Overall, the addition of an opposite-signed central vortex allows some of the peripheral vortices to move further away from the domain centre.

Of potential interest are the $N+1$-vortex arrays where the central vortex has strength $\kappa_c = -N\kappa_p$ such that the total strength of the array is zero. For $N=2$ and $N=3$, the arrays are stable ($\sigma_r^m = 0$), see the first two panels of figure 9. Figure 17 shows the maximum growth rate vs β for $N \geq 4$. In all cases the arrays are linearly unstable for all β.

The array's rotation velocity Ω vs β is given in figure 18 for the N-vortex arrays and $2 \leq N \leq 10$. As seen from equation (A.2) in the appendix, adding a central vortex of strength κ_0 modifies Ω by adding the constant term $\kappa_0/R^{\beta+2}$. Since we set $R=1$ without loss of generality, the $N+1$-vortex array may change its global rotation direction provided a negative vortex is located at the centre of the arrays with strength $\kappa_0 = \kappa_c$ less than minus the rotation velocity of the arrays of the N peripheral positive vortices.

5. CONCLUSIONS

We have investigated the stability of vortex arrays in the generalised 2D Euler's and 3D quasi-geostrophic models. We have shown that the stability of the vortex arrays depends on how fast the velocity induced by the vortices falls away from them ($u \sim r^{-(\beta+1)}$). This in turns affects the velocity shear and strain in their vicinity which conditions their stability. In the absence of a central

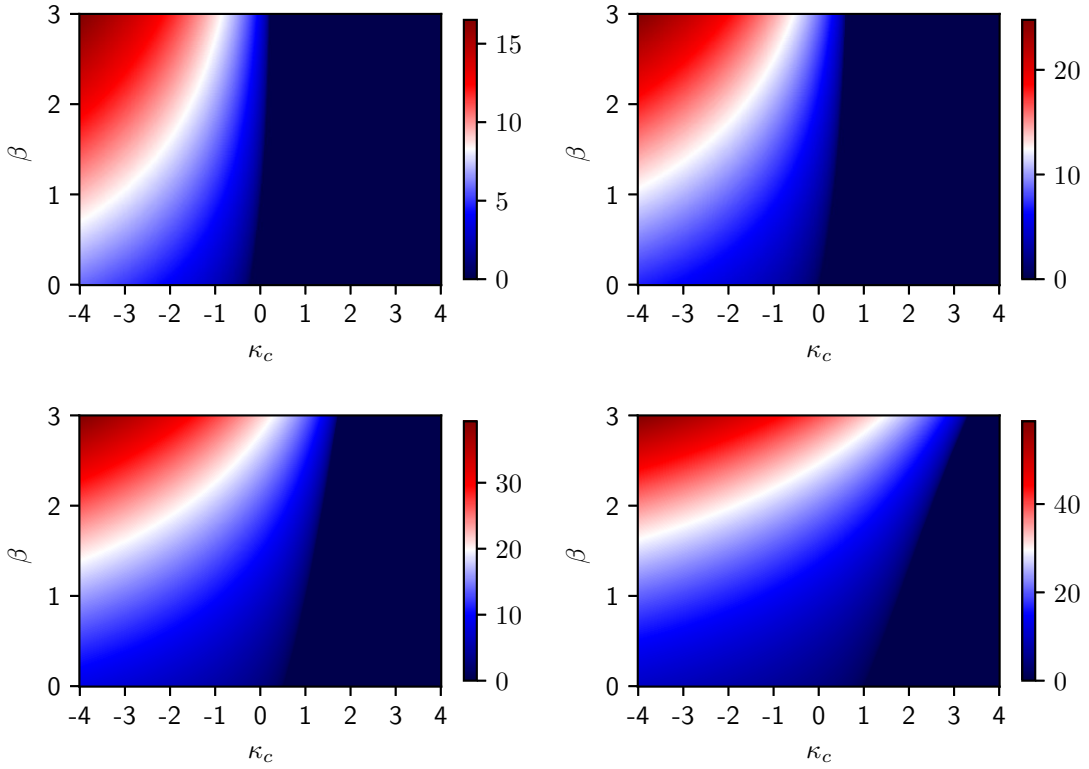

Fig. 10. Largest growth rate σ_r^m/κ_p in the (κ_c, β)-plane for a circular $N+1$-vortex array with $N = 6$ (top left), 7 (top right), 8 (bottom left) and 9 (bottom right).

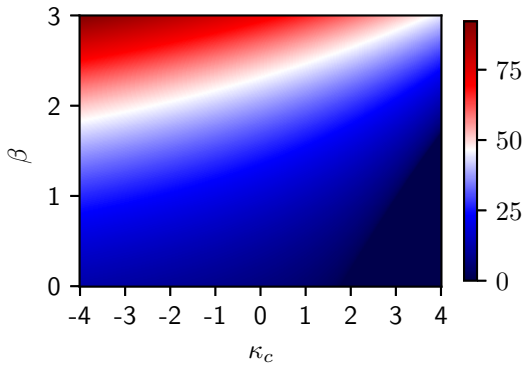

Fig. 11. Largest growth rate σ_r^m/κ_p in the (κ_c, β)-plane for a circular $10+1$-vortex array.

vortex, the circular N-vortex arrays are more unstable as the parameter β is increased. The addition of a central vortex affects the stability of the vortex arrays in a non-trivial manner. For arrays with only 2 or 3 peripheral vortices a like-signed central vortex typically destabilises the array. The effect is enhanced as β increases. On the other hand, the presence of a moderate like-signed vortex stabilises $N+1$-vortex arrays with $N \geq 4$. Intense like-signed central vortex can destabilise $N+1$ vortex arrays for $N > 5$ for small β. In such cases, increasing β stabilises the arrays.

Overall, for all β there are stable vortex arrays. These arrays are arguably the important ones in practice as they are the only ones that can form and persist in time in the flow. Other arrays can only exist as transient states, if they can exist at all, in an otherwise chaotic dynamics. These

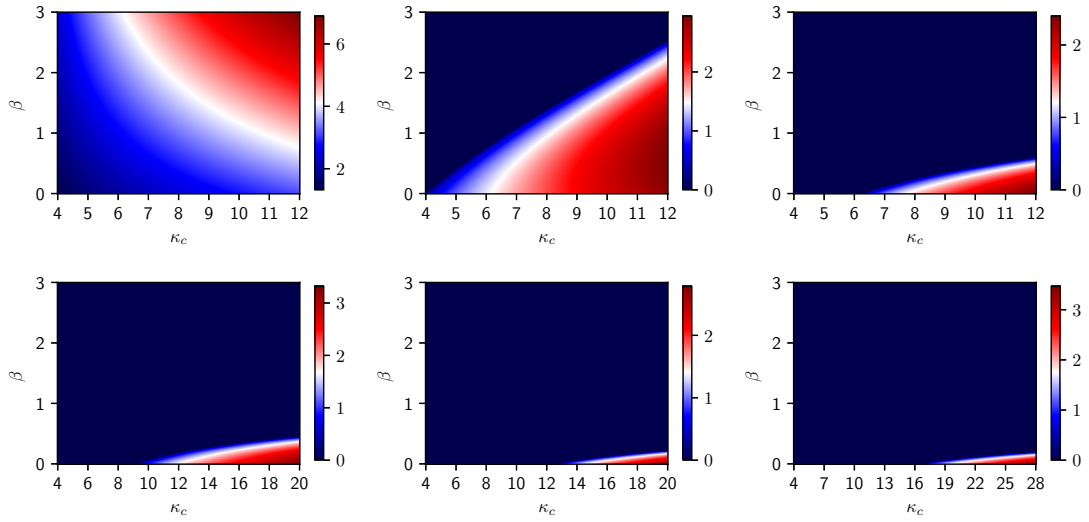

Fig. 12. Largest growth rate σ_r^m/κ_p in the (κ_c, β)-plane for a circular $N+1$-vortex array with $N=4$ (top left), 5 (top middle) 6 (top right), 7 (bottom left), 8 (bottom middle) and 9 (bottom right).

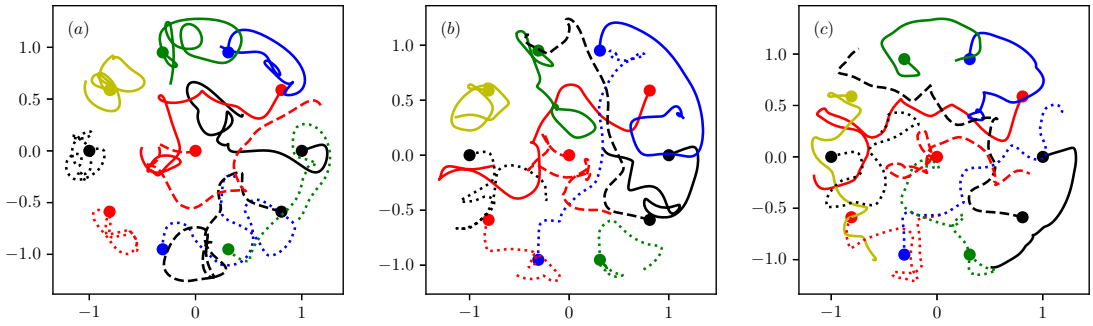

Fig. 13. Trajectories of the 11 vortices of unstable $10+1$-vortex arrays with $\kappa_c = \kappa_p$ in the reference frame steadily rotating at the equilibrium angular velocity Ω for (a): $\beta = 0.5$, $t_{max} = 4.82$, (b): $\beta = 1.5$, $t_{max} = 1.95$, (c): $\beta = 2.5$, $t_{max} = 0.94$.

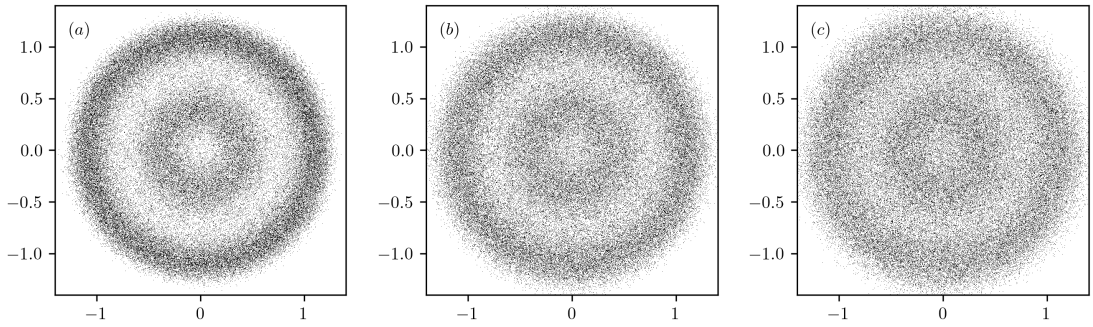

Fig. 14. Stroboscopic view of the location of vortex 1 in unstable $10+1$-vortex arrays with $\kappa_c = \kappa_p$ in the reference frame steadily rotating at the equilibrium angular velocity Ω. A point is shown every $\Delta t = 1$ for $0 \le t \le 100000$ and for (a): $\beta = 0.5$, (b): $\beta = 1.5$, (c): $\beta = 2.5$.

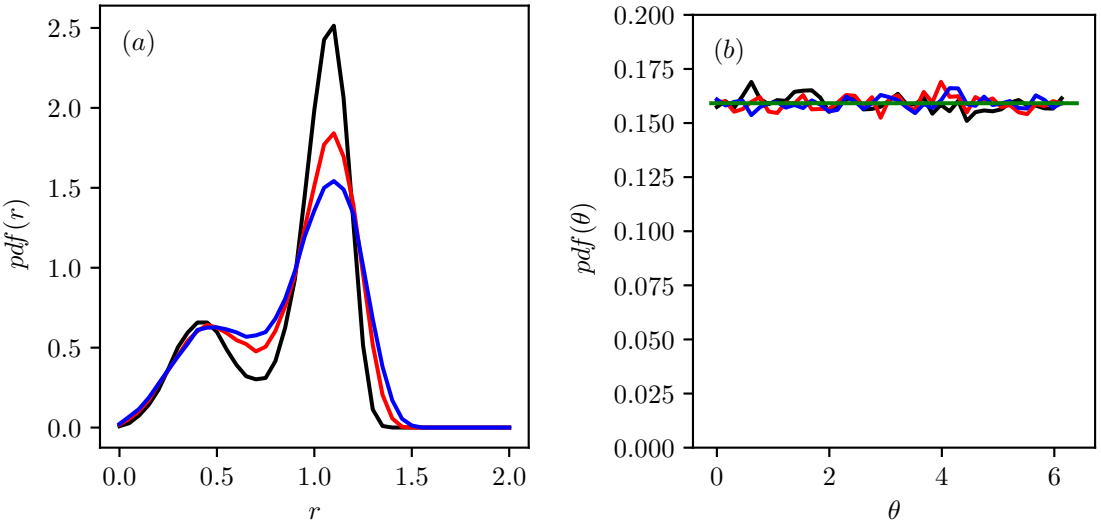

Fig. 15. *p.d.f* of radial and azimuthal location of vortex 1 in circular $10+1$-vortex arrays with $\kappa_c = \kappa_p$. The location is sampled every $\Delta t = 1$ for $0 \leq t \leq 100000$ and for $\beta = 0.5$ (solid black), $\beta = 1.5$ (solid red), $\beta = 2.5$ (solid blue). The solid green line in (b) correspond to $(2\pi)^{-1}$ corresponding to an uniform azimuthal distribution.

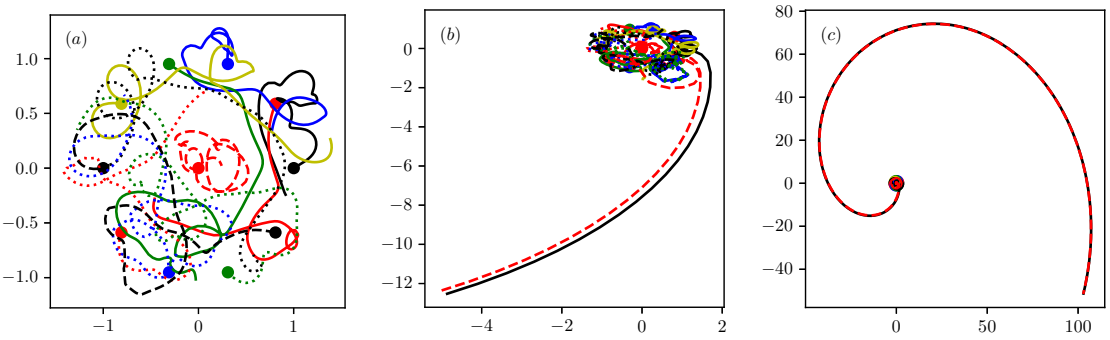

Fig. 16. Trajectories of the 11 vortices of unstable $10+1$-vortex arrays with $\kappa_c = -\kappa_p$ in the reference frame steadily rotating at the equilibrium angular velocity Ω for $\beta = 2$ and (a): $0 < t < 1$, (b): $0 < t < 1.5$, (c): $0 < t < 3$.

convoluted motions are nonetheless interesting in themselves on a purely dynamical point of view. These motions are constrained by fundamental flow invariants such as the angular impulse which can limit the region in which the vortices may evolve.

We have focused here on initial conditions which consist of arrays of vortices in mutual equilibrium. These are highly symmetric arrays. It would be interesting to explore further arrays with fewer symmetries which, instead of being in an exact mutual equilibrium may have non-trivial periodic motions and to address the stability of these motions when subject to small external perturbations.

Another possible extension is to consider the extension consist in the extension of the investigation of staggered vortex arrays considered in [8] to the generalised QG dynamics.

APPENDIX

We describe the general equations used for the linear stability analysis for the $N+1$-vortex arrays in generalised three-dimensional QG equations. For the N-vortex arrays, the equations are

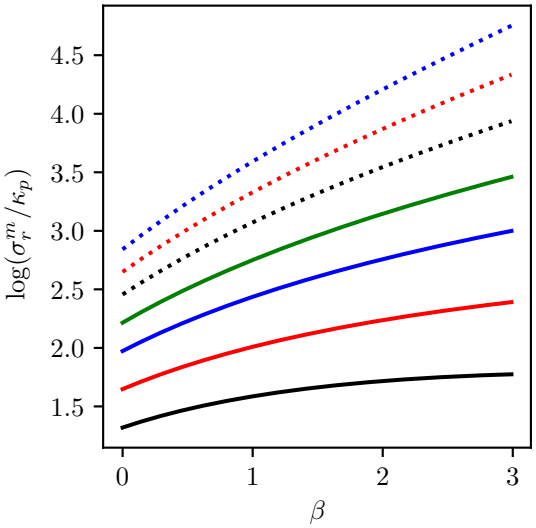

Fig. 17. Largest growth rates σ_r^m/κ_p vs β for $N = 4$ (solid black), $N = 5$ (solid red), $N = 6$ (solid blue), $N = 7$ (solid green), $N = 8$ (dotted black), $N = 9$ (dotted red) and $N = 10$ (dotted blue).

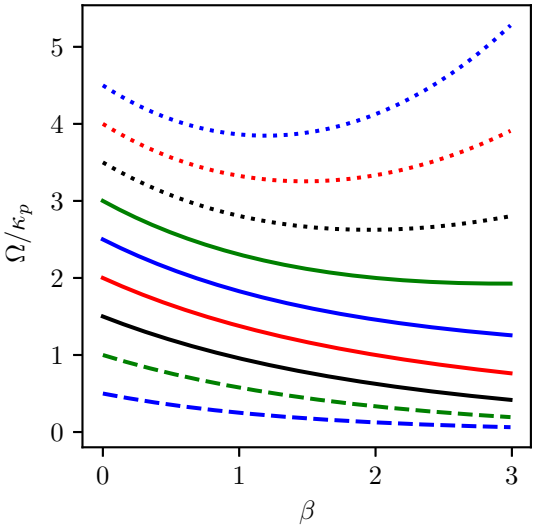

Fig. 18. Rotation vs β for $N = 2$ (dashed blue), $N = 3$ (dashed green), $N = 4$ (solid black), $N = 5$ (solid red), $N = 6$ (solid blue), $N = 7$ (solid green), $N = 8$ (dotted black), $N = 9$ (dotted red) and $N = 10$ (dotted blue).

the same just removing explicitly vortex 0 from the equations. For the two-dimensional generalised Euler equations, we simply remove the z-component in all distances. The N peripheral vortices of strength $\kappa_i = \kappa_p$, $1 \leq i \leq N$ are located along a ring of radius R at a polar angle $\{\theta_i\}_{i=1,N}$. The central vortex is located at $(0, 0, 0)$ and has strength $\kappa_0 = \kappa_c$. Note that in the present study the equations simply a little with $R = 1$ and $z_i = 0$, $\forall i$.

$$\theta_i = \frac{i-1}{N} 2\pi \tag{A.1}$$

Vortex 1 is located $(R,0,0)$ and is used to evaluate the uniform rotation angular velocity Ω

$$\Omega = \frac{v_1}{R} = \frac{\kappa_0}{R^{\beta+2}} + \sum_{i=2}^{N} \kappa_i \frac{1-\cos\theta_i}{R^{\beta+2}\left((1-\cos\theta_i)^2+\sin^2\theta_i\right)^{(\beta+2)/2}} \tag{A.2}$$

The location of the point vortices (x_i, y_i, z_i). We denote

$$r_{ij}^2 = (x_i-x_j)^2 + (y_i-y_j)^2 + (z_i-z_j)^2 \tag{A.3}$$

We consider perturbations of the horizontal position of the vortices

$$(x_i', y_i', 0) = e^{\sigma t}(\tilde{x}_i, \tilde{y}_i, 0). \tag{A.4}$$

We do not consider vertical perturbation since the vertical advection is negligible in the QG model. The equations for the perturbations are obtained by linearising the equations of motion of the vortices in the reference frame rotating with the vortices about their equilibrium position:

$$\frac{\mathrm{d}x_i'}{\mathrm{d}t} = \sigma x_i' = \Omega y_i' -$$
$$\sum_{j=0, j\neq i}^{N} \frac{\kappa_j}{r_{ij}^{\beta+2}} \left[\left(1-(\beta+2)\frac{(y_i-y_j)^2}{r_{ij}^2}\right)(y_i'-y_j') - (\beta+2)\frac{(y_i-y_j)(x_i-x_j)}{r_{ij}^2}(x_i'-x_j') \right] \tag{A.5}$$

$$\frac{\mathrm{d}y_i'}{\mathrm{d}t} = \sigma y_i' = -\Omega x_i' +$$
$$\sum_{j=0, j\neq i}^{N} \frac{\kappa_j}{r_{ij}^{\beta+2}} \left[\left(1-(\beta+2)\frac{(x_i-x_j)^2}{r_{ij}^2}\right)(x_i'-x_j') - (\beta+2)\frac{(y_i-y_j)(x_i-x_j)}{r_{ij}^2}(y_i'-y_j') \right] \tag{A.6}$$

which leads to a $(2N+2)$-eigenvalue problem where σ is the eigenvalue and $(x_0', ..., x_N', y_0', ..., y_N')$ is the eigenvector. The eigenvalue problem is numerically solved using the standard function `dgeev` of the linear algebra package Lapack.

CONFLICT OF INTEREST

The author declares that he has no conflicts of interest.

REFERENCES

1. W. Thomson. Floating magnets. *Nature*, 18:13–14, 1878.
2. A. M. Mayer. On the morphological laws of the configurations formed by magnets floating vertically and subjected to the attraction of a superposed magnet; with notes on some of the phenomena in molecular structure which these experiments may serve to explain and illustrate. *Am. J. Sci.*, 16:247–256, 1878.
3. J. J. Thomson. *A treatise of vortex rings.* MacMillan and Co., London, 1883.
4. T. H. Havelock. The stability of motion of rectilinear vortices in ring formation. *Lond. Edin. Dubl. Phil. Mag. S. 7*, 11(70):617–633, 1931. Suppl.
5. W. B. Morton. Vortex polygons. *Proc. Roy. Irish Acad.: A. Maths. Phys.*, 42:21–29, 1935.
6. L. G. Kurakin and V. I. Yudovich. The stability of stationary rotation of a regular vortex polygon. *Chaos*, 12(3), 574–595, 2002
7. G. K. Morikawa and E. V. Swenson. Interacting motion of rectilinear geostrophic vortices. *Phys. Fluids*, 14(6):1058–1073, 1971.
8. J. N. Reinaud. Three-dimensional Quasi-geostrophic Staggered Vortex Arrays. *Regul. Chaotic Dyn.*, 26(5):505–525, 2021.
9. L. G. Kurakin and I. V. Ostrovskaya. On Stability of the Thomson's Vortex N-Gon in the Geostrophic Model of the Point Bessel Vortices. *Regul. Chaotic Dyn.*, 22(7):865–879, 2017.
10. L. G. Kurakin. Stability, resonances, and instability of the regular vortex polygons in the circular domain. *Dokl. Phys.* 49:658–661, 2004.
11. L. G. Kurakin and I. .V Ostrovskaya. On the effects of circulation around a circle on the stability of a Thomson vortex N-gon. *Mathematics* 8(6):1033, 2020.

12. A. V. Borisov and A. A. Kilin. Stability of Thomson's configurations of vortices on a sphere. *Regul. Chaotic Dyn* 5:189–200, 2000.
13. H. E. Cabral and S. Boatto. Nonlinear stability of a latitudinal ring of point-vortices on a nonrotating sphere *SIAM J. Appl. Math.* 64: 26–230, 2003.
14. E. M. Artemova and A. A. Kilin. Nonlinear stability of regular vortex polygons in a Bose–Einstein condensate. *Phys. Fluids*, 33(12): 127105, 2021.
15. J. N. Reinaud. Three-dimensional quasi-geostrophic vortices equilibria with m-fold symmetry. *J. Fluid Mech.*, 863:32–59, 2019.
16. J. N. Reinaud. Finite-core quasi-geostrophic circular vortex arrays with a central vortex. *AIP Advances*, 12(2):025302, 2022.
17. J. J. Thomson. XXIV. On the structure of the atom: an investigation of the stability and periods of oscillation of a number of corpuscles arranged at equal intervals around the circumference of a circle; with application of the results to the theory of atomic structure. *Lond. Edinb. Dubl. Phil. Mag. J. Sci.*, S. 6, Vol. 7(39), 237–265, 1904.
18. D. G. Dritschel, Ring Configurations of Point Vortices in Polar Atmospheres. *Regul. Chaotic Dyn.*, 26(5):467–481, 2021.
19. G. K. Vallis. *Atmospheric and oceanic fluid dynamics: fundamentals and large-scale circulation.* Cambridge University Press, Cambridge, UK, 2006.
20. I. M. Held, R. T. Pierrehumbert, S. T. Garner, and K. L. Swanson. Surface quasi-geostrophic dynamics. *J. Fluid Mech.*, 282:1–20, 1995.
21. P. R. Stinga. User's guide to the fractional laplacian and the method of semigroups. In A. Kochubei and Y. Luchko, editors, *Partial Differential Equations*, pages 235–266. Walter De Gruyter GmbH, Berlin/Munich/Boston, 2019.
22. L. G. Khazin and E. E. Shnol. *Stability of critical equilibrium states.* Manchester University Press, New-York, Manchester, 1991.
23. A. P. Markeev. Libration Points in Celestial Mechanics and Space Dynamics. Nauka, Moscow, 1978.
24. A. N. Kunitsyn and A. P. Markeev. Stability in Resonance Cases. Surveys in Science and Engineering. General Mechanics Series, vol. 4, VINITI, Moscow, 58–139, 1979.
25. L. G. Kurakin and A. P. Melekhov and I. V. Ostrovskaya. On the stability of a regular system of the vortex charges out-side a circular domain *Izvestiya Vuzov. Severo-Kavkazskii Region. Natural Science* 4-1:24–30, 2017.